Table 1 Energy balance of a 25kw xenon lamp

	Energy, kw	%
Removed from anode	8.75	34.5
Removed from cathode	1.32	5.2
Removed by convection etc.	2.53	9.8
Radiated from arc	12.80	50.5
Total lamp input	25.40	100.0

completely avoided by this fin-type structure; however, the current capacity of the anode was not so much improved, and the anode required twice as much water flow as conventional ones. These defects of the fin-type anode are practically eliminated by adopting the multiple reciprocated-fin-type structure shown in Fig. 3. The sectional area of the center fin group is narrower than those of the either side, and the coolant flows in series through these three or more fin groups. Thus, at the center portion of the anode where the heat generation rate is high, the flow speed is high, and at the edge portions, the flow speed is relatively low. Utilizing this reciprocated-fin-type anode, the 25-kw and 30-kw lamps are developed which have enough anode heat dissipation capacity against sputtering, melting, or deformation of the anode under the rated maximum lamp inputs of 26 kw and 31 kw, respectively.

Operating Characteristics

Figure 4 shows the relation between xenon-gas pressure and lamp voltage in operation which is obtained by the test lamp with the same geometry as the 25-kw type and provided with pressure gauge. The fact that the two curves for 2.3 and 4.2 atm cold-gas pressures connect smoothly suggests that the lamp voltage depends only on the operating gas pressure but not on the lamp input. As a compromise to the contrary requirements for the lamp safety and the conversion efficiency, the average lamp voltage of 45 v, the operating xenon-gas pressure of 13 atm and the cold-gas pressure of 2.3 atm are selected for the lamps with arc gap of 12 mm from the data of Fig. 4.[4] The safety factors of the lamp bulbs for these operating conditions are estimated to be around 6.5 for operation and 80 for the cold condition, respectively. The 6.5 for operation is of the same order as the safety factors for conventional xenon short-arc lamps, which are widely used for movie projectors, but the 80 for the cold condition is much higher than those for conventional lamps, because of fairly low cold-gas pressure of 1.3 atm over normal.

The electric and radiation characteristics of the 25-kw and 30-kw lamps are shown in Figs. 5–7. Table 1 describes typical energy dissipation balance of a 25-kw arc lamp. As shown in the table, up to 50.5% of the energy conversion efficiency is obtained for 25.4-kw lamp input.

As a result of this developmental work, 25-kw and 30-kw xenon short-arc sources, as shown in Fig. 1, with at least 400 hr of service life are obtained.

References

[1] Thouret, W. E., "High-Brightness Xenon Lamps with Liquid-Cooled Electrodes," *Illuminating Engineering*, Vol. LX, No. 5, May 1965, p. 339.

[2] Leinhard, O. E., "Xenon Compact Arc Lamps with Liquid-Cooled Electrodes," *Illuminating Engineering*, Vol. LX, No. 5, May 1965, p. 348.

[3] Bartera, R. E., "Recent Solar Simulation Developments at the Jet Propulsion Laboratory," Research Report, Contract NAS 7-100, Jet Propulsion Lab., pp. 681–683.

[4] Thouret, W. E., "Tensile and Thermal Stresses in the Envelope of High Brightness High Pressure Discharge Lamps," *Illuminating Engineering*, Vol. LV, No. 5, May, 1960, p. 295.

Theoretical Penetration Mechanics of Multisheet Structures Based on Discrete Debris Particle Modeling

A. J. RICHARDSON*
Space Division of North American Rockwell, Downey, Calif.

Nomenclature†

a = area on surface of debris cloud associated with each particle
C = primary particle and first-sheet material property related to internal energy to cause fracture
d, d_c = diameters of primary and composite particles
d_1 = diameter of average particle in debris cloud
D = diameter of spherical debris cloud
D_h = diameter of hole in first sheet
E = peak internal energy in composite particle due to impact
E''' = peak internal energy per unit volume of composite particle
f = finite sheet factor
F = instantaneous force at primary particle and first-sheet interface
h = spacing between two sheets
$\bar{h}$ = sheet spacing cutoff
H_i = Brinell hardness of sheet i, kg/$\overline{mm}^2$
m_p = mass of incident primary particle
m_{p1} = mass of average particle in debris cloud
m_s = mass removed from first sheet by primary particle
n = number of particles in debris cloud
p_2 = penetration into second sheet; $p_{20} = p_2$ for $h = 0$ and/or $t_1 = 0$; $p_{21} = p_2$ for $h \geq \bar{h}$
s = distance between particles on surface of debris cloud
s = distance between leading particles on second-sheet impact
t_i = thickness of sheet i
$\bar{t}_2$ = minimum thickness of second sheet to resist perforation; $\bar{t}_{20} = \bar{t}_2$ for $h = 0$ and/or $t_1 = 0$; $\bar{t}_{21} = \bar{t}_2$ for $h \geq \bar{h}$
T = time after cloud expansion begins
$\hat{T}$ = time at which leading particles strike second sheet
V_c = velocity of center of debris cloud along X axis
$\hat{V}_{1X}$ = X component of velocity of leading particle in debris cloud
V_p = normal impact velocity of primary particle
V_{pp} = velocity of primary particle during impact
V_r = radial velocity of particles in debris cloud
V_s = velocity of material removed from first sheet during impact
X = distance cloud center has traveled
α = spacing factor for center impacts on second sheet
β = m_s/m_p
ϵ = ultimate room-temperature tensile strain of particle and first-sheet material (%)
γ = second-sheet material constant related to penetration resistance (use 0.367 for metals)
η = primary particle and first-sheet material property relating fracture energy to material temperature
ρ_p = density of primary particle
ρ = density of average particle of debris cloud
ρ_i = density of sheet i
θ = time between initial impact and formation of composite particle

Introduction

TO date, two approaches have been followed in developing penetration mechanics for multisheet meteoroid-protection systems: the theoretical approach, based upon gaseous

Presented as Paper 69-371 at the AIAA Hypervelocity Impact Conference, Cincinnati, Ohio, April 30–May 2, 1969; submitted June 16, 1969; revision received November 3, 1969. The research described was supported by North American Rockwell.

* Member of the Technical Staff, Structural Systems and Mechanisms, Research, Engineering, and Test.

† Units are in the gram, centimeter, second system unless otherwise noted.

debris cloud modeling (e.g., Madden[1] and Maiden[2]), and the empirical approach, based upon particulate debris clouds most often obtained in hypervelocity impact testing (e.g., Lundeberg[3] and Nysmith[4]). Petalling is the mode of rear-sheet failure in the first case, penetration and rear spall the mode of failure in the second. Disagreements between proponents of the two approaches have led to debates of some duration. For example, is the required second-sheet thickness proportional to projectile momentum or to projectile kinetic energy to the $\frac{1}{3}$ power? Such questions have forced analysts to make decisions they are ill-equipped to make. This Note presents a theoretical formulation based upon discrete particle debris cloud modeling intended to describe impact behavior more accurately. It is assumed that a determination has been made of the particle or range of particles to be resisted.

Debris Cloud Modeling

The debris particle size resulting from the impact of a primary particle with a thin sheet can vary drastically, depending on the combination of parameters existing at impact. In Fig. 1a, as $t_1 \rightarrow 0$, the debris particle size, d_1, must approach d. On the other hand, tests have shown that by careful selection of parameters (particularly the impact velocity and the melting point of the original particle and the shield material) one can obtain $d_1 \ll d$.

Figure 2 shows the second sheets of two-sheet targets impacted by a microparticle and a macroparticle. The microparticle test was performed by C. N. Scully of North American Rockwell's Space Division (NR SD) using a 0.002-in.-diam borosilicate glass projectile traveling at 12.7 km/sec. The first sheet was 0.0005 in. of 1100-0 aluminum, and the second sheet was 0.0015 in. of the same material. The original particle and shield material divided into approximately 500 major particles, which proceeded to crater the second sheet over a wide area. The macroparticle test was one of a series performed for NR SD by J. Jeslis at Illinois Institute of Technology Research Institute using a 0.25-in.-diam aluminum

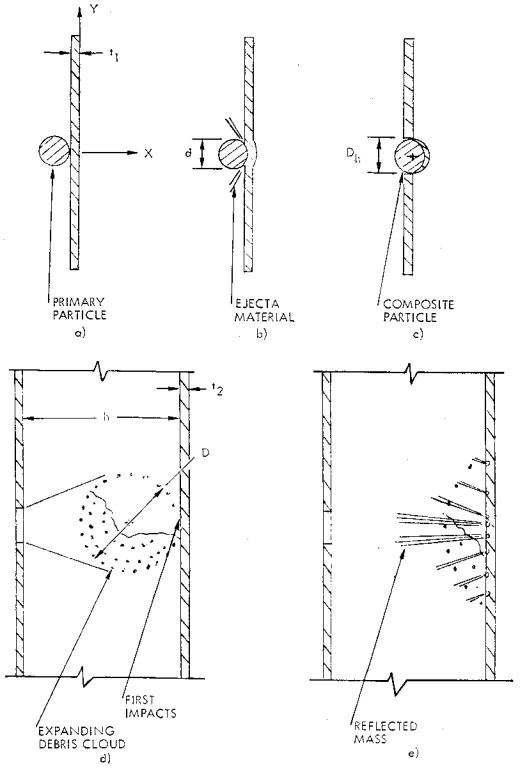

Fig. 1 Modeling of first-sheet interaction, debris cloud, and second-sheet impact.

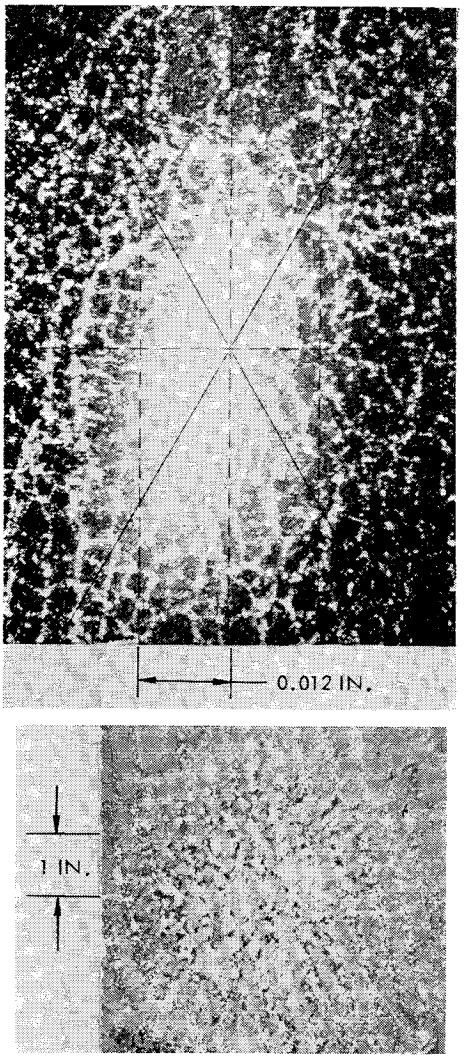

Fig. 2 Rear sheets of two-sheet aluminum targets impacted by hypervelocity microparticle (top) and by macroparticle (bottom).

sphere traveling at 7 km/sec. The target material was 2024-T3 aluminum, with first- and second-sheet thicknesses of 0.032 in. and 0.190 in. Numerous craters appeared in the second sheet. Comparing the total number of particles resulting from impacts by these particles, one observes that for similar target and projectile proportions, materials, and impact velocities, the resulting number of debris particles is comparable. One also observes that discrete debris particles are present over a wide range of impact velocities.

For an understanding of the fragmentation process, the model of Fig. 1, based on early work by Lull,[5] was employed. Here the first sheet and particle impact proceeds as follows. In Fig. 1b, the particle and target materials at the interface are ejected laterally, while the interface pressure decelerates the particle and accelerates the first-sheet material. In Fig. 1c, sheet and particle materials are traveling at the same velocity. A composite particle has been formed, and internal energy is at its peak in the form of increased pressure and temperature. In Fig. 1d, the composite particle internal energy has been converted to particle fragmentation and radial expansion of fragments. The center of the expanding spherical debris cloud travels at a velocity V_c.

For analysis, we are concerned with defining the division of the impacting particle and the shield material. Ultimately, the two must be treated separately. For now, a simpler treatment has been followed where the original particle and the shield material are partitioned into a finite number (n) of

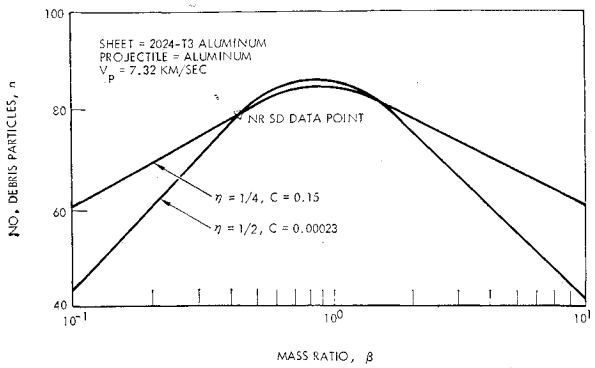

Fig. 3 Theoretical influence of mass ratio on fragmentation.

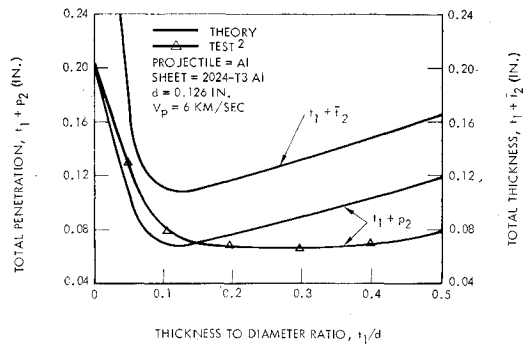

Fig. 5 Effect of first-sheet thickness on penetration of two-sheet target.

equal-size, near-spherical particles or

$$m_{p1} = (m_p + m_s)/n \tag{1}$$

where $1 \leqq n \leq \infty$, and $\rho_p = \rho_1 \equiv \rho$. The value of m_s, the mass of shield material removed, is given by

$$m_s = 0.785\rho_1 t_1 D_h^2 \tag{2}$$

where[6]

$$D_h/d = 0.658(t_1/d)^{0.14}\epsilon^{0.22}(V_p/10^5) \quad \exp[0.63(t_1/d)^{0.43}] \tag{3}$$

Preliminary work has indicated that $n = C(E''')^\eta$; if $n < 1.0$, no fragmentation occurs.

To estimate the internal energy and velocity of the particles, we neglect the material lost by ejection and forces applied to remove the mass m_s from the first sheet. In Fig. 1, we balance forces; the instantaneous interface force (F) acts on the two masses, and

$$m_p \int_{V_p}^{V_c} dV_{pp} = m_s \int_0^{V_c} dV_s = F d\theta$$

and $m_p(V_p - V_c) = m_s V_c$. Thus

$$V_c = m_p V_p/(m_s + m_p) \tag{4}$$

Next, equating the kinetic energies, one obtains

$$E = m_p m_s V_p^2/2(m_p + m_s) \tag{5}$$

The internal energy E of the composite particle now is released in partitioning of the material and as radial expansion of all particles. If all energy is allowed to be kinetic energy, the radial particle velocity is

$$V_r = V_p(m_p m_s)^{1/2}/(m_p + m_s)$$

With the introduction of

$$\beta \equiv m_s/m_p = 3D_h^2 t_1 \rho_1/2d^3\rho_p$$
$$V_r = V_p\beta^{1/2}/(1 + \beta) \tag{6}$$

The leading particles in the model debris cloud have the most penetrating capability and would have a velocity in the x direction of

$$\hat{V}_{1x} = V_r + V_c = V_p(1 + \beta^{1/2})/(1 + \beta) \tag{7}$$

When Eq. (5) is used, the specific internal energy of the composite particle is

$$E''' = \rho E/(m_s + m_p) = \rho\beta V_p^2/2(1 + \beta)^2 \tag{8}$$

When this is combined with $n = C(E''')^\eta$, the relationship for fragmentation becomes

$$n = C[\rho\beta V_p^2/2(1 + \beta)^2]^\eta \tag{9}$$

Next, establish the location of each particle within the debris cloud. Let all particles be uniformly distributed on the surface of a sphere of diameter D. The variation of D with time is

$$D = d_c + 2V_r T(x) \tag{10}$$

When Eq. (4) is used, the time for the cloud center to travel a distance X is $T(X) = X/V_c = X(1 + \beta)/V_p$. Then

$$D = d_c + 2X\beta^{1/2} \tag{11}$$

The sphere area associated with each particle is

$$a = \pi(d_c + 2X\beta^{1/2})^2/n \tag{12}$$

From these latter equations, the dispersion of the secondary particles onto a second sheet can be determined.

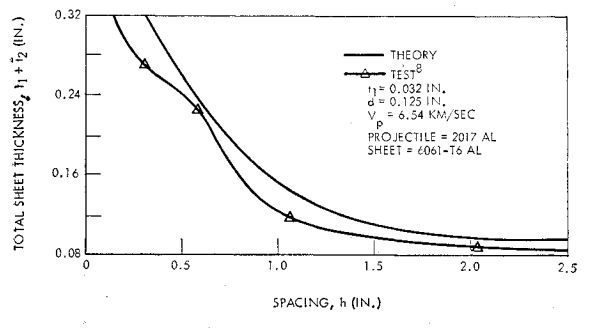

Fig. 4 Effect of spacing on two-sheet structures.

Cloud Interaction With Second Sheet

Referring to Fig. 1e, if t_2 is spaced far enough from t_1, all the particles will act independently and become miniature reproductions of the original particle impact. This is an efficient form of two-sheet structure. The model employed will show the particles closely grouped at the center of impact on the second sheet and thinly dispersed at the extremity of the impact area on a second sheet, which corresponds to the test results of Fig. 2. The distance between the leading particles is

$$s = a^{1/2} = (\pi/n)^{1/2}(d_c + 2X\beta^{1/2}) \tag{13}$$

For the case where X is large relative to d_c, Eq. (13) reduces to $s \simeq 2(\pi\beta/n)^{1/2}X$. The time required for the leading particle to cover the distance h is $\hat{T} = h/\hat{V}_{1x}$. The position of the cloud at this time is $X = \hat{T}V_c = hV_c/\hat{V}_{1x}$. Thus, the minimum distance between impacts on the second sheet is

$$\hat{s} \cong 2(\pi\beta/n)^{1/2}hV_c/\hat{V}_{1x} \tag{14}$$

The impacts of the particles at the rear of the cloud are neglected because of their reduced energy and wide scatter. Making substitutions, one obtains

$$\hat{s} = 2(\pi\beta/n)^{1/2}h/(1 + \beta^{1/2}) \tag{15}$$

Since we wish to have a certain second-sheet area associated

with each particle to stop the particle with a minimum-thickness second sheet, s should be several times diameter d_1. Let $\hat{s} = \alpha d_1$. Since

$$d_1 = (6m_{p1}/\pi\rho)^{1/3} = [6m_p(1 + \beta)/\pi\rho n]^{1/3} \quad (16)$$

then

$$\hat{s} = \alpha[6m_p(1 + \beta)/\pi\rho n]^{1/3} \quad (17)$$

Equating Eqs. (15) and (17), solve for the spacing $\bar{h}$ to achieve maximum spacing effect and obtain minimum second-sheet thickness

$$\bar{h} = 0.282d\alpha n^{1/6}(1 + \beta)^{1/3}(1 + \beta^{1/2})/\beta^{1/2} \quad (18)$$

As one would expect, Eq. (18) indicates that as $n \to \infty$, $\bar{h}$ should also go to infinity to provide a free area for impact of each of n particles. Certainly, it may be difficult to provide extremely large spacings on the spacecraft. On the other hand, the spacing required changes slowly with n. Also, as n becomes very large, the particle can be stopped by an infinitely thin second sheet, which in itself is a solution to the meteoroid shielding problem.

From previous work,[7] the penetration into the second sheet by a single particle is

$$p_{21} = 8.15 \times 10^{-4} m_{p1}{}^{\gamma}\rho^{1/2-\gamma}\hat{V}_{1X}{}^{2/3}/H_2{}^{1/4}\rho_2{}^{1/6}$$

and the minimum thickness of the second sheet required to resist perforation may be expressed as

$$\bar{t}_{21} = fp_{21} \quad (19)$$

Substituting for m_{p1} and V_{1X}, one obtains

$$p_{21} = 8.15 \times 10^{-4}\left(\frac{m_p}{n}\right)^{\gamma}\frac{[1 + \beta^{1/2}]^{2/3}}{(1 + \beta)^{2/3-\gamma}}\frac{V_p{}^{2/3}\rho^{1/2-\gamma}}{\rho_2{}^{1/6}H_2{}^{1/4}}h \geqq \bar{h} \quad (20)$$

The value of second-sheet penetration for the case $h = 0$ is given by

$$p_{20} = \frac{8.15 \times 10^{-4} m_p{}^{\gamma}\rho^{1/2\ -\gamma}V_p{}^{2/3}}{H_2{}^{1/4}\rho_2{}^{1/6}} - t_1\left(\frac{H_1}{H_2}\right)^{1/4}\left(\frac{\rho}{\rho_2}\right)^{1/6} \quad (21)$$

$$h = 0$$

and the corresponding second-sheet thickness is

$$\bar{t}_{20} = fp_{20},\ h = 0 \quad (22)$$

Values for intermediate spacings can be determined by interpolation. Equations (21) and (22) apply also to the case where t_1 goes to 0.

Application and Correlation

Some of the equations derived have been applied to sizing of two-sheet structures and the following design considerations were identified. When sizing structures (and meteoroid protection), one should be particularly interested in the effect of the first-sheet thickness on particle division, and Eq. (9) can be applied to determine trends for various materials and impact velocities. As indicated, β (rather than t_1) is the significant parameter; the maximum n should occur when $\beta = 1$. With data from early test shots against two-sheet 2024-T3 aluminum targets, the materials constants were tentatively established as $\eta = \frac{1}{4}$, $C = 0.15$, $f = 1.8$, and $\alpha = 10.0$. (The shallower curve in Fig. 3 applies for the conditions indicated.)

The β dependence of Eq. (9) should apply for the case when $\rho_p \neq \rho_1$. Therefore, t_1 should be chosen to provide $\beta \simeq 1$ for this case also. This finding provides theoretical support to experimental findings that the optimum t_1 is not a constant times d for all combinations of particle and first-sheet materials as thought earlier but, instead, is influenced strongly by the material combinations chosen.

Increased sheet spacing reduces second-sheet damage only up to the cutoff spacing $\bar{h}$ where the particles act independently; further spacing increase does not reduce the required t_2. The value of $\bar{h}$ can be determined from Eq. (18), wherein the important parameter is the h/d ratio rather than the spacing itself. Figure 4 compares the theory with a correlation of the test data of Ref. 8. Equations (19–22) were applied to determine the variations of total penetration and total sheet thickness with t_1/d (Fig. 5). The correlation with test data obtained is encouraging. Note that the low points of the curves are in the vicinity of $t_1/d = 0.1$ to 0.2, corresponding to $\beta = 1.0$.

The equations can be applied to obtain considerably more information on two-sheet structures. The discrete particle theory has been extended to more complex configurations and has proven to be a powerful aid to the understanding of penetration mechanics of three-sheet structures and structures containing insulation.

As noted in the introduction, two modes of rear-sheet failure must be considered: penetration plus rear spall and bulge and tear. The foregoing method treats the first mode. In spacecraft analysis, the second mode of failure also should be checked. The debris cloud modeling described has been applied to this case also through consideration of the impulse loading on the second sheet and the resulting energy absorption by bulging.

References

[1] Madden, R., "Ballistic Limit of Double-Walled Meteoroid Bumper System," TN D-3916, April 1967, NASA.

[2] Maiden, C. J. et al., "Thin Sheet Impact," TR 64-61, Nov. 1964, General Motors, Goleta, Calif.

[3] Lundeberg, J. F. et al., "Meteoroid Protection for Spacecraft Structures," CR-54201, Oct. 1965, NASA.

[4] Nysmith, C. R., "Penetration Resistance of Double-Sheet Structures at Velocities to 8.8 km/sec," TN D-4568, May 1968, NASA.

[5] Lull, D. B., "Analysis of Impact of Hypervelocity Pellet With a Thin Shield," Rept. ASRL 99-1, *Survey of Hypervelocity Impact Information*, edited by W. Herrmann and A. H. Jones, Sept. 1961, Massachussets Institute of Technology.

[6] McHugh, A. H., "Evaluation of Hypervelocity Impact Damage to a Thin Sheet by Multiple Regression Analysis," STR 152, June 1966, Space Div., North American Rockwell, Downey, Calif.

[7] Richardson, A. J. and McHugh, A. H., "Hypervelocity Impact Penetration Equation for Metal by Multiple Regression Analysis," STR 153, March 1966, Space Div., North American Rockwell, Downey, Calif.

[8] Swift, H. F. et al., "Ballistic Limits of 6061-T6 Aluminum Bumper Systems," TR 67-324, Oct. 1967, Air Force Materials Lab., Wright-Patterson Air Force Base, Dayton, Ohio.

Thermal Coupling of Equipment by Interleaving Fins

SIDNEY GROSS*

The Boeing Company, Seattle, Wash.

THERMAL radiation is employed extensively in space applications for temperature control of internal components.[1,2] However, radiation is often a weak method of thermal coupling, because the rates of heat transfer are much lower than attainable by conduction. Interleaving fins can significantly increase the rate of heat transfer by increasing the effective area per unit base area The concept (Fig. 1) consists of hot fins radiating to colder fins in counter-direction.

Received August 7, 1969; revision received December 31, 1969.

* Engineer, Aerospace Systems Division.